Gas-Phase Synthesis of Tunable-Size Germanium Nanocrystals by Inert Gas Condensation

Zhu, Xiaotian; ten Brink, Gert H.; de Graaf, Sytze; Kooi, Bart J.; Palasantzas, George

Published in:
Chemistry of Materials

DOI:
10.1021/acs.chemmater.9b05076

Publication date:
2020

CHEMISTRY OF MATERIALS

pubs.acs.org/cm

Article

Gas-Phase Synthesis of Tunable-Size Germanium Nanocrystals by Inert Gas Condensation

Xiaotian Zhu, Gert H. ten Brink, Sytze de Graaf, Bart J. Kooi, and George Palasantzas*

Cite This: *Chem. Mater.* 2020, 32, 1627−1635

Read Online

ACCESS | Metrics & More | Article Recommendations | Supporting Information

ABSTRACT: Size-dependent optical properties of germanium (Ge) nanocrystals (NCs) make them a desirable material for optoelectronic applications. So far, the synthesis of ligand-free and tunable-size Ge NCs by inert gas condensation has been scarcely reported. In this work, we introduce a gas-phase approach to synthesize quantum-confined Ge NCs by inert gas condensation, where the size of the Ge NCs can be readily tuned by controlling the thickness of a Cu plate supporting the Ge target. As explained by simulations using the finite element method, the magnetic field configuration above the target can be manipulated by varying the thickness of the Cu backing plate. In-depth analysis based on transmission electron microscopy (TEM) results reveals the morphology and crystalline structure of Ge NCs. X-ray photoelectron spectroscopy has proven the formation of a substoichiometric Ge oxide shell for the as-deposited Ge NCs. In addition, Raman spectroscopy indicated peak shifts according to the phonon confinement model that yielded nanoparticle sizes in a good agreement with the TEM results. Furthermore, the quantum confinement effect for Ge NCs was demonstrated by analysis of the absorption (UV−vis−NIR) spectrum, which indicated that the band gap of the Ge NCs was increased from ∼0.8 to 1.1 eV with decreasing size of Ge NCs. Comparison with theory shows that the quantum confinement effect on the band gap energy for different-sized Ge NCs follows the tight-binding model rather well.

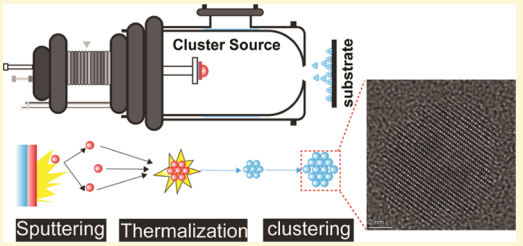

INTRODUCTION

Nowadays, semiconductor nanocrystals (NCs) with size less than the Bohr exciton radius, or quantum dots (QDs) as they are called in the literature, have gained strong interest due to the dependence of their physical properties on the so-called quantum confinement effect, where the band gap energy of the materials can be engineered by the size reduction of the NCs.[1] Based on size-dependent optical and electrical properties, semiconductor NCs are emerging candidates that enable a wide range of important applications, e.g., solar cells,[2] light-emitting devices,[3] and photodetectors.[4] Although the binary II−VI, IV−VI, and III−V semiconductor nanocrystals are well developed and remain at the forefront of several developing technologies, group IV semiconductor NCs have also attracted strong attention as potential alternatives, leading to intense research. The main interest arises from the fact that, in contrast to several quantum dot systems that contain toxic elements, as, for example, Cd and Pb, group IV semiconductor NCs are environmentally friendly and cost efficient.[5] In addition, group IV semiconductor NCs (Si and Ge) are compatible with the current CMOS processing based on the Si technology.[6] Although Si remains of high interest for optoelectronics applications, germanium (Ge) is especially attractive due to: (i) the narrower bulk band gap energy (0.67 eV at 300 K) that implies possible tuning to specific wavelengths over a wide range (as much as 3.3 eV); (ii) the relatively larger Bohr exciton radius (∼24 nm) than that of Si (4.5 nm) that translates to quantum confinement effects for larger NCs than Si NCs; (iii) the significant potential for indirect to direct (or quasi-direct) transitions that could be achieved at nanoscale ranges; (iv) a larger dielectric constant and a large absorption coefficient (∼2 × 10^5 cm^{-1} at 2 eV);[7] and (v) carrier multiplication for approximately 5−6 nm Ge NCs.[8]

The strategies to synthesize Ge NCs can be clearly grouped into two major categories: solution-phase and gas-phase routes. In recent years, many solution-phase methods, including Zintl salts,[9] sol−gel process,[10,11] microwave-assisted colloid reduction,[12−14] reduction of GeI_2,[15] and solution-phase thermal decomposition,[16,17] have been reported. However, in contrast to the gas-phase methods, the production of high-quality group IV NCs has been proven to be difficult by solution-phase methods.[18,19] One of the main reasons is the high crystallization temperature of Ge NCs due to the strong covalent bonding of Ge,[20] which means that the choice of organic solvents will be limited by their boiling point.[21] In addition, in some cases, the use of strong reducing agents (e.g., $NaBH_4$ and $LiAlH_4$ superhydrides), which are environmentally unfriendly, cannot be avoided.[21] Another issue is the use of surfactants, which serve as a stabilizer of NCs in the solution. Moreover, since these organic surface ligands can also produce

Received: December 9, 2019
Revised: January 24, 2020
Published: January 24, 2020

photoluminescence, the interpretation of the band gap energy from photoluminescence spectra can, in some cases, conceal the genuine signal originating from the size effect of the semiconductor NCs.[21,22] To our knowledge, only a few works have shown that the energy of the photoluminescence peak increases with decreasing size of the Ge NCs, which is induced by the quantum confinement effect instead of surface ligands.[23−26] In contrast, the gas-phase routes are not limited by any use of organic solvents, reducing agents, and surfactants, which is desirable for the green and high-purity synthesis of NCs. Overall, the advantages of the gas-phase method are: (i) readily synthesizing NCs for high covalent materials like Si and Ge; (ii) excluding the use of solvents and ligands; and (iii) easily achieving size control. A wide variety of possibilities are available for the gas-phase synthesis of NCs,[27] such as cluster beam deposition,[28−30] nonthermal plasma,[31,32] laser pyrolysis,[33] and thermal plasmas.[34] Recently, several advances have emerged from gas-phase synthesis of NCs from the IV group via nonthermal plasma.[35,36] In this case, the size of Ge NCs could be controlled by varying the flow rate and employing a Grignard reaction that allowed the surface passivation with alkyl groups instead of Cl groups. Ge NCs with different sizes demonstrated tunable band gap photoluminescence due to the quantum confinement effect.[23]

Besides the nonthermal plasma method, the cluster beam deposition is a promising method for the synthesis of high-quality semiconductor NCs. In particular, the inert gas method based on high-pressure magnetron sputtering[30] has emerged as one of the most versatile approaches to control the particle formation processes, where, especially, the size distribution can be tuned by the dynamical parameters of the magnetron source, such as the magnetic field configuration, power, flow of inert gas (Ar, He), and length of the aggregation zone.[37] However, the literature for utilizing the cluster source in the synthesis of semiconductor NCs still remains rather limited since only a few publications[38,39] so far have reported this possibility for semiconductor QDs. Nevertheless, the main deficiency of the current research is on how to control the morphology of the semiconductor nanoparticles, since they often adopt a "cauliflower" structure. Although such structures consist of smaller nanoparticles, they do not agree with monodisperse and size-tunable semiconductor NCs and are therefore less suited for optoelectronic applications requiring high-quality semiconductor QDs.

Therefore, significant progress is required toward the size and morphology control of Ge NCs via the gas-phase synthesis based on high-pressure magnetron sputtering.[30] Hence, in this work, we report a gas-phase synthesis based on high-pressure magnetron sputtering that provides Ge NCs with 100% tunable size, ranging from 14.7 to 7.1 nm, enabling significant band gap engineering. For this purpose, we studied extensively the influence of backing plates of different thicknesses on the magnetic strength above the Ge target surface, where the main focus is on the size-tunable synthesis of Ge NCs. The finite element method (FEM) was used to simulate the magnetic field distribution, suggesting that the magnetic field strength above the target surface decreases with increasing thickness of the backing plate, enabling the desired size tuning of the Ge NCs. This strategy eliminates the need for quadrupole mass filter to achieve size selection and thereby significantly increases the effective yield of nanoparticles out of the system. Furthermore, it will be shown that the as-deposited Ge NCs have a monodisperse and uniform size distribution with a band gap that widens with decreasing size as expected from quantum confinement calculations.

EXPERIMENTAL AND SIMULATION METHODS

Synthesis of Ge NCs. Germanium (Ge) nanocrystals (NCs) with different sizes were deposited on transmission electron microscopy (TEM) grids by a home-modified nanoparticle deposition system Nanogen 50 obtained from Mantis Deposition Ltd. (www.mantisdepositon.com). The main chamber, where the samples are placed, was initially evacuated to a base pressure of $\sim 1 \times 10^{-8}$ mbar. The supersaturated Ge vapor was produced by sputtering the Ge target (50.8 mm diameter, 3 mm thickness, purity of 99.99%) with a 20 sccm Ar gas flow (purity 99.9999%) and a 0.20 A discharge current. The supersaturated vapor was then cooled by Ar gas to form nuclei, which can subsequently grow into nanoparticles. The formed NCs in the aggregation chamber were then carried by the Ar gas to the sample chamber. For nanoparticles of different sizes, various copper backing plates (diameter 50.8 mm and thickness varying between 1.5 and 6 mm) were used as a separation between the Ge target and the magnetron head. The latter can adjust the magnetic field strength on the target surface, where sputtering takes place. To synthesize a large amount of NCs for further characterization, the precleaned glass substrate was put close to the aperture at the exit of the aggregation chamber (Figure 2a).

Materials Characterization. The morphology, size distribution, and electron diffraction of the as-deposited NCs were analyzed by transmission electron microscopy (TEM, JEOL 2010) operated at 200 kV. High-resolution TEM (HRTEM) was performed with a probe- and image-corrected Thermo Fisher Scientific Themis Z S/TEM operating at 300 kV. The high-angle annular dark-field scanning transmission electron microscopy (HAADF-STEM) images were recorded with a convergence semiangle of 21 mrad and a beam current of 50 pA. The composition of NCs was further characterized by X-ray photoelectron spectroscopy (XPS, Surface Science SSX-100 ESCA instrument) with a monochromatic Al K_α X-ray source ($h\nu$ = 1486.6 eV) operating at a base pressure of $\sim 5 \times 10^{-10}$ mbar. The NCs were directly deposited on a substrate coated by a 150 nm thick film of gold. The electron takeoff angle with respect to the surface normal was 37°, the diameter of the analyzed area was 1000 μm, and the total experimental energy resolution was set to 1.16 eV. The XPS spectra were analyzed by the least-squares curve fitting program (Winspec, developed at the LISE laboratory of the University Notre-Dame de la Paix, Namur, Belgium). The binding energies (BEs) are reported with a precision of ±0.1 eV and referenced with respect to the C 1s (BE = 285.6 eV) photoemission peak. Finally, Raman spectra were collected from NC films deposited on silicon substrates. The Raman spectra were recorded on a Raman microscope (Thorlabs HNL) using the 632 nm line of a He−Ne laser as the excitation wavelength, at approximately 2.5 mW in the range of 200−2000 cm^{-1}. The optical absorption of the NCs was obtained by a Shimadzu UV3600 spectrometer. To avoid the thickness effect in further measurements, the samples for both Raman spectra and UV−vis−NIR spectroscopy were deposited simultaneously to keep the same deposition conditions.

Finite Element Method (FEM) Simulation. The magnetic field configuration and the race track, which develops during sputtering on the Ge target, were modeled by the finite element method (FEM) via the commercial software COMSOL Multiphysics. The magnetic and electric field module of COMSOL Multiphysics was adopted for simulating the magnetic field of the cluster source for the modified nanoparticle deposition Nanogen 50. The magnetic flux densities and the magnetic field strength $B_{//}$ ($\sqrt{B_x^2 + B_y^2}$) were calculated from the simulation results, with the *XY* plane considered parallel to the target surface. Moreover, the configuration and materials of the simulation model were assigned with the corresponding value of the specific cluster source, and the ambient condition was set as the vacuum. The exterior boundary condition in this simulation was used as the zero magnetic scalar potential condition. To get an accurate simulation, a

https://dx.doi.org/10.1021/acs.chemmater.9b05076
Chem. Mater. 2020, 32, 1627−1635

particularly fine mesh was selected for the magnetron source. Since the nonmagnetic Ge target was used for deposition, the shape and strength of the magnetic field configuration cannot be influenced. Therefore, the magnetic flux densities ($B_{//}$) on the target surface were calculated based on the total thickness (target and backing plate) above the copper shield of the magnetron head (Scheme 1).

Scheme 1. Schematic Diagram of the Cluster Deposition Source for Ge NCs as Based on High-Pressure Magnetron Sputtering

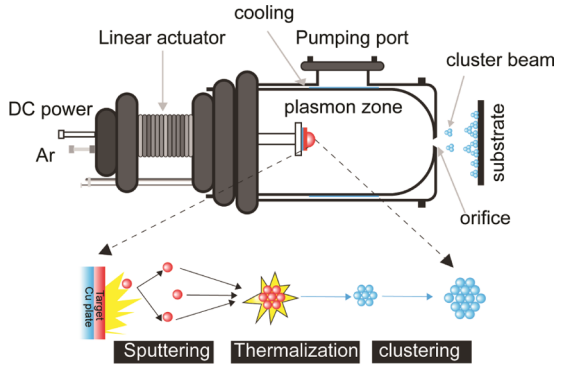

RESULTS AND DISCUSSION

Morphology and Size Control of Ge NCs. Figure 1a–d shows bright-field TEM images of differently sized Ge NCs,

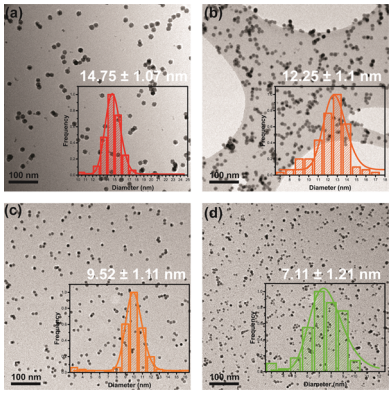

Figure 1. (a–d) Bright-field TEM images of as-deposited Ge NCs having different sizes as produced by a cluster source based on high-pressure magnetron sputtering using different thicknesses (δ) of the backing plates: (a) δ = 0 cm, (b) δ = 1.5 cm, (c) δ = 2 cm, and (d) δ = 3 cm. (e) Average diameter of Ge NCs at various thicknesses of the backing plate. Insets: size histograms of the Ge NCs with curves fitted to the log-normal size distribution model.

which exhibit isolated pseudospherical structures. The corresponding size distribution analysis is shown in the insets of Figure 1a–d, which demonstrates that the average size can be tuned from 14.7 to 7.1 nm by varying the thickness of the backing plate. The reason for the size tunability of the NCs is that the backing plate thickness directly affects the plasma density, which is strongly related to the NCs growth rate. Any change in the backing plate distance between the target and magnetron effectively changes the magnetic field strength of the magnetron. During magnetron sputtering, as shown in Scheme 1, plasma confinement is achieved above the target surface with the help of the magnetron. In the plasma region, collisions between electrons and gas atoms (Ar or He) result in the ionization of the sputtering gas forming excited species (Ar^+ or He^+). Subsequently, the accelerated gas ions impact on the Ge target, resulting in the emission and formation of the cluster seed that strongly affects the cluster production rate and size.[40] Since a stronger magnetic field confinement results in higher ionization, and a lower diffusion rate of atoms away from the source region, the sputtering can be achieved at a high rate with the dense plasma, leading to larger cluster sizes.[41] Therefore, using a thick backing plate can lead to a weaker magnetic field strength above the target surface.[42]

To evaluate the variation of magnetic field strength by changing the thickness of backing plates, FEM simulations of the commercial magnetron source were performed. Figure 2b–

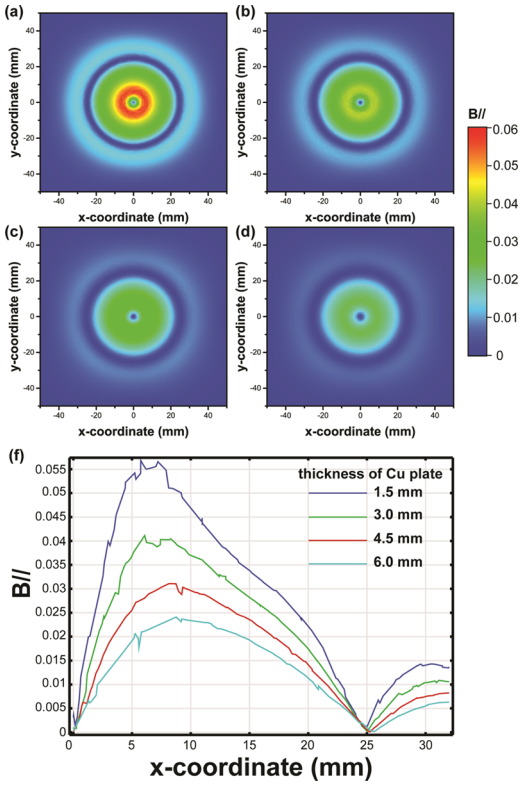

Figure 2. (a–d) Simulated results of the magnetic field strength ($B_{//}$) for different thicknesses of Cu plate: (a) 1.5 mm, (b) 3.0 mm, (c) 4.5 mm, and (d) 6.0 mm. (e) $B_{//}$ profile of the magnetic field along the radial direction for the four axial distances.

e shows the shape and magnitude of the $B_{//}$ ($\sqrt{B_x^2 + B_y^2}$) field on the XY plane of the target surface, when four different thicknesses (1.5, 3.0, 4.5, 6.0 mm) of the backing plates were used with the z-coordinate set to 4.5, 6.0, 7.5, and 9.0 mm in multislice, respectively. Similarly, Figure 2f depicts the profiles of the magnetic field distribution as a function of radial distances along the target surface. Due to the radial symmetry, the profiles in Figure 2f provide a direct representation of Figure 2b–e. Figure 2 thus clearly shows that the magnetic flux density decreases with increasing axial outward distance. As a result, the electron confinement becomes less tight and a wider race track is expected. Since the supersaturation can be achieved only by sufficient confinement of the vapor, individual atoms or very small clusters will be deposited with reduced magnetic flux density. According to the FEM results, the magnetic field strength can be controlled by the thickness of

https://dx.doi.org/10.1021/acs.chemmater.9b05076
Chem. Mater. 2020, 32, 1627–1635

backing plates, which, in turn, governs the confinement of electrons and, consequently, can modulate the size of the Ge NCs. For synthesizing smaller (<7 nm) Ge NCs, a substantial Cu plate is required. However, then it is difficult to achieve a stable plasma confinement because the magnetic field strength on the Ge target surface becomes too weak. Zhao et al. indicated that the synthesis of smaller Si NCs can be achieved by increasing the amount of inert drift gas (in particular, He) because the drift velocity can then be raised, which causes the residence time of clusters in the aggregation volume to decrease. Nevertheless, in this case, an amorphous structure is anticipated for smaller Si NCs. Notably, a critical ratio of the number density of the Si and Ar atoms (ρ_{Si}/ρ_{Ar}) is needed to heat the Si NCs over the crystallization temperature during the condensation process.[43]

Structural Characterization of Ge NCs. As we report in Figure 3, the HRTEM characterization was performed in conjunction with the selective area electron diffraction (SAED) to reveal the crystalline details of the Ge NCs. The diffraction pattern in Figure 3b demonstrates that the crystalline structure of Ge NCs can be indexed with the diamond cubic ($Fd3m$) structure, as the measured interplanar distances of Ge d_{111}, d_{022}, and d_{113} are 0.326, 0.198, and 0.169 nm, respectively. Figure 3c shows exemplary single-crystal Ge NCs oriented along a [212] zone axis. The fast Fourier transform (FFT) in Figure 3d verifies the diamond cubic crystal structure, containing the (111), (220), and (311) characteristic reflections. Using the line profiles for the (111) and (022) interplanar spacings of Ge NCs, as shown in Figure 3e, the d-spacings were calculated to be 1.98 Å for (022) and 3.26 Å for (111). This is in agreement with the spacing distances measured from the SAED pattern. In addition to the majority (~60%) single-crystal Ge NCs (as shown in Figure S2), also particles with a polycrystalline structure, oxidation shell, and partially amorphous substructure were identified in the HAADF-STEM images of all samples (Figure 3f–h). This is attributed to the intrinsically high crystallization temperature and oxidation of Ge. Specifically, as Figure 3f illustrates, as-deposited Ge NCs can also contain a single twin boundary, as indicated by the yellow dashed line. The corresponding FFT pattern demonstrates that the angle between these two domains is around 40°. In fact, such an incomplete crystalline structure of the Ge NCs has been recognized as the major reason that progress in the preparation and further optoelectronic application for group IV NCs has fallen behind those of the group II–VI and III–V NCs.[24,44,45] Moreover, due to the existence of the oxidation layer, and the partially amorphous structure, the Ge NCs contain many trap states for photogenerated charge carriers that increase the probability of nonradiative recombination.[23,46] As an additional measurement of the material composition, energy-dispersive X-ray spectra were measured and typical Ge peaks were observed (see Supporting Information Figure S1).

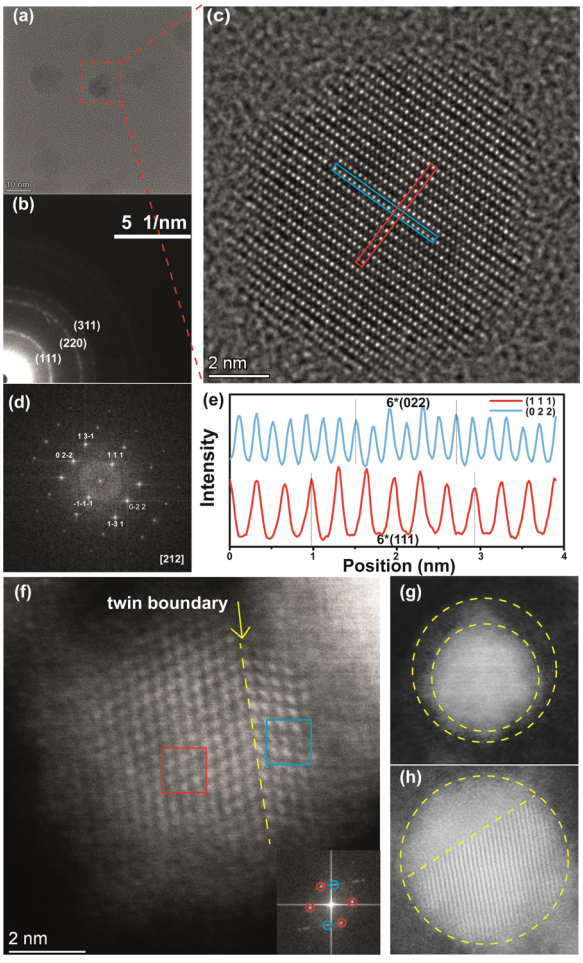

Figure 3. Representative HRTEM micrographs of Ge NCs: (a) overview of the as-deposited Ge NCs, (b) electron diffraction pattern confirming the diamond cubic crystalline structure of Ge NCs, (c) HRTEM image of Ge NCs taken along a [212] zone axis, (d) line profile along the red and blue lines in the HRTEM image of (c), (e) corresponding FFT analysis of the HRTEM image along the [212] zone axis in (c), (f) twin crystalline structure of Ge NCs, (g) oxidation, and (h) partially amorphous Ge NCs.

Further analysis of the stoichiometry and chemical valence for the as-deposited Ge NCs was carried out by X-ray photoelectron spectroscopy (XPS). The survey spectra (Figure 4a) demonstrate only the presence of Ge, O, and C in the as-deposited Ge NCs. Figure 4b shows the high-resolution XPS spectra of the Ge 3d core-level region. Due to a non-negligible fraction of Ge NCs bonded with O, a broad emission peak centered at 29.4 eV can be seen. To quantitatively analyze the valence of the as-deposited Ge NCs, the spectra were fitted by multiple Voigt functions. The three main components can be seen at 29.2, 30.5, and 32.0 eV peaks. The emission peak at 29.2 eV is attributed to the Ge–Ge bonds involved in the QD formation. Other higher-energy peaks are related to the presence of GeO (30.5 eV) and GeO_2 (32.0 eV). In addition, the results of the integrated peak area, which are related to each valence state, indicate that the majority components are ~54.0% as Ge, ~31.0% as GeO, and ~15.0% as GeO_2.

Raman Spectroscopy. The vibrational properties of the as-deposited Ge NCs with different sizes were also characterized by Raman spectroscopy. Since only optical phonons located at the center of the Brillouin zone are involved in the first-order Raman scattering process for an infinite Ge crystal, there is no momentum exchange during the Raman scattering that leads to a sharp and symmetric vibrational peak at 300 cm^{-1}. However, according to the phonon confinement model,[47,48] the nanoparticles can be considered as a finite crystal and the phonon can be described by a wave packet (instead of plane wave) whose spatial dimensions are commensurate with the crystallite size. As a result, the Raman-active modes will be shifted away from the

https://dx.doi.org/10.1021/acs.chemmater.9b05076
Chem. Mater. 2020, 32, 1627–1635

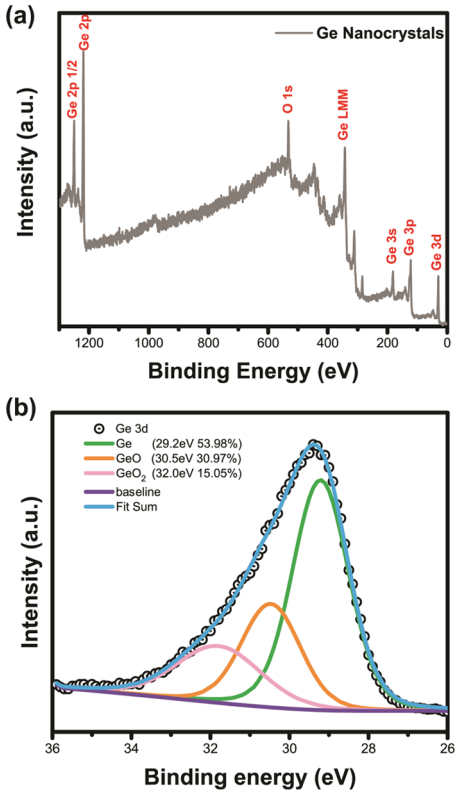

Figure 4. XPS spectra of a typical Ge NCs: (a) survey spectrum and (b) high-resolution peak of Ge 3d valence level showing three different fitted Voigt peaks representing Ge, GeO, and GeO_2, with Ge being dominant.

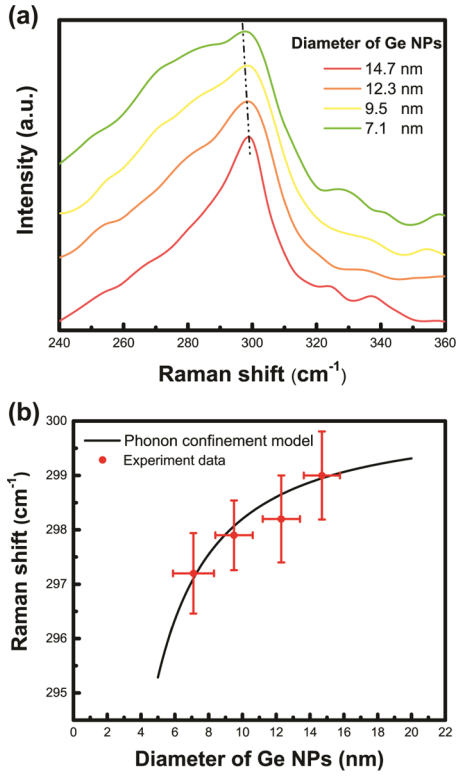

Figure 5. (a) Raman spectra of the Ge NCs with four different average diameters. (b) Raman shift of the peak position as a function of the diameter of Ge NCs.

Brillouin zone center by an effective offset $\Delta q = \sim\pi/D$, where D is the diameter of Ge NCs. Consequently, the Raman peak will be asymmetrically broadened and will shift to lower wavenumbers with decreasing nanoparticle size. Indeed, the first-order Raman spectrum can be described by the phonon confinement model

$$I(\omega) = \int \frac{|C(0, \mathbf{q})|^2 d^3\mathbf{q}}{[\omega - \omega(\mathbf{q})]^2 + (\Gamma_0/2)^2} \quad (1)$$

In eq 1, $C(0,\boldsymbol{q})$ is the Fourier coefficient of the weighting function that can be considered nearly constant, $\boldsymbol{q}$ is expressed in units of $2\pi/a_{Ge}$, where a_{Ge} is the lattice constant of Ge (0.568 nm), $\omega(\boldsymbol{q})$ is the phonon dispersion curve, and Γ_0 is the Raman natural line width of bulk Ge.

Figure 5a shows the typical Raman spectra for the Ge NCs with the four different sizes. According to the phonon confinement model, smaller NCs will lead to a shift of the Raman peak to lower wavenumber and also the development of a broader and asymmetric peak (as shown in Figure 5a). The low-frequency tail of the broad Ge−Ge optical phonon peak can be interpreted as stemming not only from changes in the bond length (due to the increased surface-to-volume ratio of smaller NCs, the fraction of shorter bond lengths from the uncoordinated surface atoms will be increased, which induces Raman scattering at lower frequencies)[14] but also by the existence of the amorphous state or lower crystallinity for smaller NCs, as shown in Figure 3f−h. To analyze the relationship between the frequency downshift $\Delta\omega(D)$ of the Raman peak and the diameter D of Ge NCs, the phonon confinement model can be simplified by the bond polarizability model[49] that leads to the power-law behavior

$$\Delta\omega(D) = -A(a/D)^{\gamma} \quad (2)$$

where a is the lattice parameter of Ge (0.5658 nm). The parameters A and γ are used to describe the vibrational confinement due to the finite size for the Ge NCs. These parameters have the values $A = -97.462$ cm^{-1} and $\gamma = 1.39$ for nanometric spheres of diameter D.[46] According to the peak position in Figure 5a, the size of the Ge NCs can be obtained by the phonon confinement model yielding for D the values 15.2, 10.0, 8.95, and 7.28 nm. The differences in the diameter of as-deposited Ge NCs between the calculated results from eq 2 and TEM results (cf. Figure 1) are presented in Table 1.

Table 1. Comparison the Size of Ge NCs between the Results from TEM and the Fitting Results of Phonon Confinement Model

	crystallite size (nm)			
D_{TEM}	14.75	12.25	9.52	7.11
D_{PCM}	15.20	10.00	8.95	7.28
$\Delta D = \lvert D_{TEM} - D_{PCM} \rvert$	0.45	2.25	0.57	0.17

Indeed, although for one size a relatively large error occurred, the other values show a good consistency between the Raman and TEM measurements for the Ge NCs. The size deviation between the TEM and Raman results can be explained by underestimating the percentage of bigger Ge NCs in the TEM data. This is because, to obtain the size distribution, the instrumental correction of the TEM data tends to underestimate the percentage of bigger Ge NCs in favor of the more

https://dx.doi.org/10.1021/acs.chemmater.9b05076
Chem. Mater. 2020, 32, 1627−1635

numerous smaller NCs.[50] In addition, the peak shift of the optical Ge−Ge phonon demonstrates that the states of Ge NCs preserve their individual character instead of forming bulk Ge films. Finally, as Figure 5b shows, the calculation of the Raman shifts using eq 2 with D the values obtained from the TEM (Table 1) indicates a good agreement with the measured Raman frequency shifts.

Confinement Effects Due to Size-Dependent Optical Properties of Ge NCs. Furthermore, the optical properties of the Ge NCs were investigated via UV−vis−NIR absorbance measurements. Unlike the direct band gap semiconductors, such as the PbS, the photoluminescence signal for the Ge NCs could not be easily observed limiting the precise determination of the band gap of the NCs. Holman et al. also indicated that the blue-shifted photoluminescence data in many papers originate from the surface ligand on the Ge NCs.[22] Until now, only four reports present convincing photoluminescence data yielding a band gap energy close to that of bulk Ge with increasing size of the Ge NCs.[23−26] According to the quantum confinement effects, when the size of semiconductor nanocrystals is below the Bohr exciton radius (~24 nm for Ge), the size-dependent effect will manifest itself by band gap broadening of the Ge NCs.[21] As it is shown in Figure S3a, with decreasing size of the Ge NCs, the onset of the absorption peak undergoes a blue shift that follows very well the predicted trend of quantum confinement effects. Notably, the quantum confinement theory suggests that because of the geometric restriction of charge carriers at the nanoscale, the momentum conservation could be relaxed for optical transitions.[16] As a result, the probability of band-to-band transition (quasi-direct) can be improved for indirect band gap semiconductor nanocrystals.[21] However, the exciton peak cannot be observed in the absorption spectra for our experiments, suggesting that no conversion occurs from indirect to quasi-direct band gap structure for the Ge NCs (see also Supporting Information Figure S3b).

To analyze more quantitatively the size effects on optical band gaps from absorption spectra, Tauc plots were made[51,52] since this is a common method to interpret the optical band gap for semiconductor materials from the absorption spectrum. The band gap energies can be determined by extrapolating the tangential line from the linear region of the onset of the first major absorption to the intersection point of the abscissa on the energy axis. The approximate indirect band gap energies of the Ge NCs from the Tauc plots (see Figure 6a) were 0.85 eV for 14.7 nm, 0.95 eV for 12.3 nm, 1.06 eV for 9.5 nm, and 1.12 eV for 7.1 nm. These band gap energies suggest strong quantum size effects when the size of the Ge NCs is smaller than the Bohr exciton radius and a clear trend of widening band gap with decreasing size of Ge NCs. However, the absorption measurements lack the correction of light scattering, which makes it difficult to identify precisely the absorption onset.[14]

To illustrate the confinement effect of Ge NCs, we summarized the band gap energies as a function of the NCs size along with the data from studies of other groups,[23,24,53] as shown in Figure 6b. In addition, the relationship between the band gap energy and the size of the Ge NCs was also compared to the effective mass model (EMM)[54,55] and a tight-binding (TB) model.[56] In the strong confinement regime, where the size of NCs is smaller than the Bohr radius (~24 nm), the relationship between the band gap energy $E_{g,NC}$ and the particle diameter D based on the EMM is given by

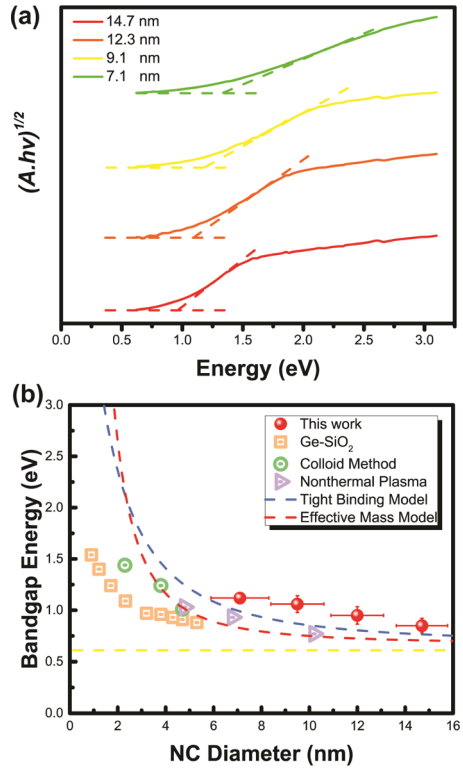

Figure 6. (a) Tauc plot from the absorption data used to determine the band gap energy of Ge NCs. (b) Comparison with band gap size versus nanoparticle diameter data from the literature. The band gap energies determined in this work are plotted together with the ones of Ge NCs synthesized with the colloidal method,[24] Ge NCs embedded in SiO_2,[53] Ge NCs synthesized with the nonthermal plasma method,[23] and predicted band gap values obtained from an effective mass and a tight-binding (TB) model.

$$E_{g,NC} = E_{g,bulk} + \frac{h^2}{2D^2}\left(\frac{1}{m_e^*} + \frac{1}{m_h^*}\right) \quad (3)$$

where $E_{g,bulk}$ is the bulk band gap energy of Ge (0.67 eV), h is the Planck constant, and m_e^* and m_h^* are the effective masses of the electrons and holes, respectively. If the effective mass can be calculated using the density of states, then the mass term in eq 3 can be correlated with the parabolicity of the band structure. The latter means that the bulk effective mass value of Ge can be used for the nanostructures. Therefore, these definitions yield from eq 3 for the band gap of the NCs

$$E_{g,NC} = E_{g,bulk} + \frac{A}{D^2} \quad (4)$$

where the calculated parameter A for Ge is 7.88 eV × nm^2.[54,57]

The band gap from the sp^3 TB model for spherical dots can be described by the analytic expression[56]

$$E_{g,NC} = E_{g,bulk} + \frac{11863.7}{D^2 + 2.397D + 4.252} + \frac{15143.8}{D^2 + 6.465D + 2.546} \quad (5)$$

Since the EMM is known to overestimate the band gap energy of NCs as small as a few nanometers,[53] a more accurate theoretical description can be obtained by the TB model. As it is shown in Figure 6b, our experimentally resolved band gap shows a clear dependence on the size of Ge NCs and a similar

https://dx.doi.org/10.1021/acs.chemmater.9b05076
Chem. Mater. 2020, 32, 1627−1635

trend to that predicted by the TB model. In addition, we observe that all our experimental results are higher than the prediction of the TB model. Such a slight difference can be explained by several deficiencies such as surface oxidation, defects in crystalline Ge clusters, and partly amorphous Ge clusters. First, the XPS analysis has shown that the as-deposited Ge NCs cannot be expected to be a pure ensemble of Ge NCs. Indeed, the effect of substoichiometric oxide shells on the shift of the band gap energy has been reported in the literature.[58] Second, as it is also mentioned in the HRTEM characterization of the NCs, the deviation of the band gap energy may also result from the existence of an uncertain fraction of incomplete crystallites or defects within the Ge NCs. Third, because of the band gap energy determination by extrapolation from the optical absorption tail, the uncertainty in the interpretation of the optical spectrum could also be the source of the error.[59] In any case, the good agreement with the TB model suggests that the as-deposited Ge NCs persist to exhibit the indirect band gap nature also in the quantum confinement regime.

CONCLUSIONS

In summary, a novel gas-phase synthesis procedure for Ge NCs has been established via the gas aggregation cluster source that allows a relatively simple way to tune the size and subsequently the optical absorption of Ge NCs. The size selection can readily be controlled by the adjustment of the equivalent thickness of the target (using various thicknesses for the backing plate) that allows manipulation of the magnetic field configuration on the target surface as it has been explained in terms of the FEM simulations. Therefore, one can avoid the use of mass selection to form size-selected NCs and thus avoid sacrificing the production yield of NCs. HRTEM and Raman spectroscopy demonstrated in close agreement that the size of Ge NCs decreases with increasing equivalent thickness of the Ge target. HRTEM and SAED measurements demonstrated that most Ge NCs have a single crystalline diamond structure. HRTEM also revealed the presence of an oxide shell, as well as more details of the crystalline structure as, for example, the existence of a minor fraction of NCs with a polycrystalline structure. In addition, the XPS study verified the valence state of the Ge NCs and quantified the number of the oxidation states of the NCs indicating substoichiometric Ge oxide shells. Furthermore, the data from the UV−vis absorbance measurements demonstrated via the Tauc plots the quantum confinement effect on the band gap of Ge NCs showing a band gap energy that can be tuned by the size of Ge NCs. Finally, we stress that our results follow the TB model prediction for the band gap size rather well. Although high-quality Ge NCs without oxidation and with a homogeneous crystalline phase are still challenging to produce, the cluster deposition method shown here can readily produce tunable-size solid-state Ge NCs, which is promising for further solid-state optoelectronic device investigations. Currently, research is in progress to suppress the oxidation and improve the crystalline quality during deposition, as well as to combine the synthesis with other group IV nanoparticles (e.g., GeSi and GeSn). In addition, our method might also be suitable for other highly covalent systems (e.g., InN or InSb), which could be difficult to synthesize by the solution-phase method.[18]

ASSOCIATED CONTENT

Supporting Information

The Supporting Information is available free of charge at https://pubs.acs.org/doi/10.1021/acs.chemmater.9b05076.

EDS spectrum of the Ge NCs; HR-STEM images of single-crystal Ge NCs; absorption spectrum of the Ge NCs and Tauc plots of the spectrum using both direct and indirect band gap parameters; and plots to indicate the absence of the Urbach tail for the Ge NCs samples (PDF)

AUTHOR INFORMATION

Corresponding Author

George Palasantzas − *Zernike institute for Advanced Materials, University of Groningen 9747 AG Groningen, The Netherlands;* orcid.org/0000-0002-5084-8769

Authors

Xiaotian Zhu − *Zernike institute for Advanced Materials, University of Groningen 9747 AG Groningen, The Netherlands*

Gert H. ten Brink − *Zernike institute for Advanced Materials, University of Groningen 9747 AG Groningen, The Netherlands*

Sytze de Graaf − *Zernike institute for Advanced Materials, University of Groningen 9747 AG Groningen, The Netherlands*

Bart J. Kooi − *Zernike institute for Advanced Materials, University of Groningen 9747 AG Groningen, The Netherlands*

Complete contact information is available at: https://pubs.acs.org/10.1021/acs.chemmater.9b05076

Notes

The authors declare no competing financial interest.

ACKNOWLEDGMENTS

X.Z. gratefully acknowledges the financial support from China Scholarship Council (CSC, No. 201707040079). All authors thank the support from the Zernike Institute for Advanced Materials. They thank Prof. Dr. Maria Antonietta Loi (University of Groningen) for the use of the UV−vis−NIR spectroscopy and Mustapha Abdu-Aguye (University of Groningen) for assistance with the measurement.

REFERENCES

(1) Efros, A. L.; Lockwood, D. J.; Tsybeskov, L. *Semiconductor Nanocrystals: From Basic Principles to Applications*; Springer: New York, 2013.

(2) Nozik, A. J.; Beard, M. C.; Luther, J. M.; Law, M.; Ellingson, R. J.; Johnson, J. C. Semiconductor Quantum Dots and Quantum Dot Arrays and Applications of Multiple Exciton Generation to Third-Generation Photovoltaic Solar Cells. *Chem. Rev.* **2010**, *110*, 6873−6890.

(3) Keuleyan, S.; Lhuillier, E.; Brajuskovic, V.; Guyot-Sionnest, P. Mid-Infrared HgTe Colloidal Quantum Dot Photodetectors. *Nat. Photonics* **2011**, *5*, 489−493.

(4) Shirasaki, Y.; Supran, G. J.; Bawendi, M. G.; Bulović, V. Emergence of Colloidal Quantum-Dot Light-Emitting Technologies. *Nat. Photonics* **2013**, *7*, 13−23.

(5) Carolan, D.; Doyle, H. Size and Emission Color Tuning in the Solution Phase Synthesis of Highly Luminescent Germanium Nanocrystals. *J. Mater. Chem. C* **2014**, *2*, 3562−3568.

(6) Vaughn, D. D.; Schaak, R. E. Synthesis, Properties and Applications of Colloidal Germanium and Germanium-Based Nanomaterials. *Chem. Soc. Rev.* **2013**, 2861−2879.

(7) Philipp, H. R.; Taft, E. A. Optical Constants of Germanium in the Region 1 to 10 Ev. *Phys. Rev.* **1959**, *113*, 1002−1005.

(8) Saeed, S.; de Weerd, C.; Stallinga, P.; Spoor, F. C.; Houtepen, A. J.; Siebbeles, L. D.; Gregorkiewicz, T. Carrier Multiplication in Germanium Nanocrystals. *Light Sci. Appl.* **2015**, *4*, No. e251.
(9) Taylor, B. R.; Kauzlarich, S. M.; Lee, H. W. H.; Delgado, G. R. Solution Synthesis of Germanium Nanocrystals Demonstrating Quantum Confinement. *Chem. Mater.* **1998**, *10*, 22−24.
(10) Henderson, E. J.; Seino, M.; Puzzo, D. P.; Ozin, G. A. Colloidally Stable Germanium Nanocrystals for Photonic Applications. *ACS Nano* **2010**, *4*, 7683−7691.
(11) Henderson, E. J.; Hessel, C. M.; Veinot, J. G. C. Synthesis and Photoluminescent Properties of Size-Controlled Germanium Nanocrystals from Phenyl Trichlorogermane-Derived Polymers. *J. Am. Chem. Soc.* **2008**, *130*, 3624−3632.
(12) Muthuswamy, E.; Zhao, J.; Tabatabaei, K.; Amador, M. M.; Holmes, M. A.; Osterloh, F. E.; Kauzlarich, S. M. Thiol-Capped Germanium Nanocrystals: Preparation and Evidence for Quantum Size Effects. *Chem. Mater.* **2014**, *26*, 2138−2146.
(13) Muthuswamy, E.; Iskandar, A. S.; Amador, M. M.; Kauzlarich, S. M. Facile Synthesis of Germanium Nanoparticles with Size Control: Microwave versus Conventional Heating. *Chem. Mater.* **2013**, *25*, 1416−1422.
(14) Tabatabaei, K.; Holmes, A. L.; Newton, K. A.; Muthuswamy, E.; Sfadia, R.; Carter, S. A.; Kauzlarich, S. M. Halogen-Induced Crystallinity and Size Tuning of Microwave Synthesized Germanium Nanocrystals. *Chem. Mater.* **2019**, *31*, 7510−7521.
(15) Lu, X.; Korgel, B. A.; Johnston, K. P. High Yield of Germanium Nanocrystals Synthesized from Germanium Diiodide in Solution. *Chem. Mater.* **2005**, *17*, 6479−6485.
(16) Zaitseva, N.; Dai, Z. R.; Grant, C. D.; Harper, J.; Saw, C. Germanium Nanocrystals Synthesized in High-Boiling-Point Organic Solvents. *Chem. Mater.* **2007**, *19*, 5174−5178.
(17) Gerung, H.; Bunge, S. D.; Boyle, T. J.; Brinker, C. J.; Han, S. M. Anhydrous Solution Synthesis of Germanium Nanocrystals from the Germanium(II) Precursor Ge[N(SiMe3)2]2. *Chem. Commun.* **2005**, *14*, 1914−1916.
(18) Lu, H.; Carroll, G. M.; Neale, N. R.; Beard, M. C. Infrared Quantum Dots: Progress, Challenges, and Opportunities. *ACS Nano* **2019**, 939−953.
(19) Rodio, M.; Scarpellini, A.; Diaspro, A.; Intartaglia, R. Tailoring of Size, Emission and Surface Chemistry of Germanium Nanoparticles via Liquid-Phase Picosecond Laser Ablation. *J. Mater. Chem. C* **2017**, *5*, 12264−12271.
(20) Fan, J.; Chu, P. K. Group IV Nanoparticles: Synthesis, Properties, and Biological Applications. *Small* **2010**, *6*, 2080−2098.
(21) Carolan, D. Recent Advances in Germanium Nanocrystals: Synthesis, Optical Properties and Applications. In *Progress in Materials Science*; Pergamon, 2017; pp 128−158.
(22) Holman, Z. C.; Kortshagen, U. R. Absolute Absorption Cross Sections of Ligand-Free Colloidal Germanium Nanocrystals. *Appl. Phys. Lett.* **2012**, *100*, No. 133108.
(23) Wheeler, L. M.; Levij, L. M.; Kortshagen, U. R. Tunable Band Gap Emission and Surface Passivation of Germanium Nanocrystals Synthesized in the Gas Phase. *J. Phys. Chem. Lett.* **2013**, *4*, 3392−3396.
(24) Ruddy, D. A.; Johnson, J. C.; Smith, E. R.; Neale, N. R. Size and Bandgap Control in the Solution-Phase Synthesis of near-Infrared-Emitting Germanium Nanocrystals. *ACS Nano* **2010**, *4*, 7459−7466.
(25) Heath, J. R.; Shiang, J. J.; Alivisatos, A. P. Germanium Quantum Dots: Optical Properties and Synthesis. *J. Chem. Phys.* **1994**, *101*, 1607−1615.
(26) Lee, D. C.; Pietryga, J. M.; Robel, I.; Werder, D. J.; Schaller, R. D.; Klimov, V. I. Colloidal Synthesis of Infrared-Emitting Germanium Nanocrystals. *J. Am. Chem. Soc.* **2009**, *131*, 3436−3437.
(27) Kruis, F. E.; Fissan, H.; Peled, A. Synthesis of Nanoparticles in the Gas Phase for Electronic, Optical and Magnetic Applications—a Review. *J. Aerosol Sci.* **1998**, *29*, 511−535.
(28) Sattler, K.; Mühlbach, J.; Recknagel, E. Generation of Metal Clusters Containing from 2 to 500 Atoms. *Phys. Rev. Lett.* **1980**, *45*, 821−824.
(29) Pratontep, S.; Carroll, S. J.; Xirouchaki, C.; Streun, M.; Palmer, R. E. Size-Selected Cluster Beam Source Based on Radio Frequency Magnetron Plasma Sputtering and Gas Condensation. *Rev. Sci. Instrum.* **2005**, *76*, No. 045103.
(30) Haberland, H.; Mall, M.; Moseler, M.; Qiang, Y.; Reiners, T.; Thurner, Y. Filling of Micron-sized Contact Holes with Copper by Energetic Cluster Impact. *J. Vac. Sci. Technol., A* **2002**, *12*, 2925−2930.
(31) Kortshagen, U. R.; Sankaran, R. M.; Pereira, R. N.; Girshick, S. L.; Wu, J. J.; Aydil, E. S. Nonthermal Plasma Synthesis of Nanocrystals: Fundamental Principles, Materials, and Applications. *Chem. Rev.* **2016**, *116*, 11061−11127.
(32) Ahadi, A. M.; Hunter, K. I.; Kramer, N. J.; Strunskus, T.; Kersten, H.; Faupel, F.; Kortshagen, U. R. Controlled Synthesis of Germanium Nanoparticles by Nonthermal Plasmas. *Appl. Phys. Lett.* **2016**, *108*, No. 093105.
(33) Ehbrecht, M.; Huisken, F. Gas-Phase Characterization of Silicon Nanoclusters Produced by Laser Pyrolysis of Silane. *Phys. Rev. B* **1999**, *59*, 2975−2985.
(34) Rao, N.; Girshick, S.; Heberlein, J.; McMurry, P.; Jones, S.; Hansen, D.; Micheel, B. Nanoparticle Formation Using a Plasma Expansion Process. *Plasma Chem. Plasma Process.* **1995**, *15*, 581−606.
(35) Wheeler, L. M.; Nichols, A. W.; Chernomordik, B. D.; Anderson, N. C.; Beard, M. C.; Neale, N. R. All-Inorganic Germanium Nanocrystal Films by Cationic Ligand Exchange. *Nano Lett.* **2016**, *16*, 1949−1954.
(36) Jurbergs, D.; Rogojina, E.; Mangolini, L.; Kortshagen, U. Silicon Nanocrystals with Ensemble Quantum Yields Exceeding 60%. *Appl. Phys. Lett.* **2006**, *88*, No. 233116.
(37) Palmer, R. E.; Cai, R.; Vernieres, J. Synthesis without Solvents: The Cluster (Nanoparticle) Beam Route to Catalysts and Sensors. *Acc. Chem. Res.* **2018**, *51*, 2296−2304.
(38) Tang, W.; Eilers, J. J.; Van Huis, M. A.; Wang, D.; Schropp, R. E. I.; Di Vece, M. Formation and Photoluminescence of "Cauliflower" Silicon Nanoparticles. *J. Phys. Chem. C* **2015**, *119*, 11042−11047.
(39) Cardoso, J.; Marom, S.; Mayer, J.; Modi, R.; Podestà, A.; Xie, X.; van Huis, M. A.; Di Vece, M. Germanium Quantum Dot Grätzel-Type Solar Cell. *Phys. Status Solidi A* **2018**, *215*, No. 1800570.
(40) Marek, A.; Valter, J.; Kadlec, S.; Vyskočil, J. Gas Aggregation Nanocluster Source — Reactive Sputter Deposition of Copper and Titanium Nanoclusters. *Surf. Coatings Technol.* **2011**, *205*, S573−S576.
(41) Vernieres, J.; Steinhauer, S.; Zhao, J.; Chapelle, A.; Menini, P.; Dufour, N.; Diaz, R. E.; Nordlund, K.; Djurabekova, F.; Grammatikopoulos, P.; et al. Gas Phase Synthesis of Multifunctional Fe-Based Nanocubes. *Adv. Funct. Mater.* **2017**, *27*, No. 1605328.
(42) Xing, L.; ten Brink, G. H.; Kooi, B. J.; Palasantzas, G. Preparation of Tunable-Sized Iron Nanoparticles Based on Magnetic Manipulation in Inert Gas Condensation (IGC). *J. Appl. Phys.* **2017**, *121*, No. 024305.
(43) Zhao, J.; Singh, V.; Grammatikopoulos, P.; Cassidy, C.; Aranishi, K.; Sowwan, M.; Nordlund, K.; Djurabekova, F. Crystallization of Silicon Nanoclusters with Inert Gas Temperature Control. *Phys. Rev. B* **2015**, *91*, No. 035419.
(44) Wang, W.; Huang, J.; Ren, Z. Synthesis of Germanium Nanocubes by a Low-Temperature Inverse Micelle Solvothermal Technique. *Langmuir* **2005**, *21*, 751−754.
(45) Kortshagen, U. Nonthermal Plasma Synthesis of Semiconductor Nanocrystals. *J. Phys. D. Appl. Phys.* **2009**, *42*, No. 113001.
(46) Ghosh, B.; Hamaoka, T.; Nemoto, Y.; Takeguchi, M.; Shirahata, N. Impact of Anchoring Monolayers on the Enhancement of Radiative Recombination in Light-Emitting Diodes Based on Silicon Nanocrystals. *J. Phys. Chem. C* **2018**, *122*, 6422−6430.
(47) Nemanich, R. J.; Solin, S. A.; Martin, R. M. Light Scattering Study of Boron Nitride Microcrystals. *Phys. Rev. B* **1981**, *23*, 6348−6356.
(48) Campbell, I. H.; Fauchet, P. M. The Effects of Microcrystal Size and Shape on the One Phonon Raman Spectra of Crystalline Semiconductors. *Solid State Commun.* **1986**, *58*, 739−741.

https://dx.doi.org/10.1021/acs.chemmater.9b05076
Chem. Mater. 2020, 32, 1627−1635

(49) Zi, J.; Büscher, H.; Falter, C.; Ludwig, W.; Zhang, K.; Xie, X. Raman Shifts in Si Nanocrystals. *Appl. Phys. Lett.* **1996**, *69*, 200−202.
(50) Bottani, C. E.; Mantini, C.; Milani, P.; Manfredini, M.; Stella, A.; Tognini, P.; Cheyssac, P.; Kofman, R. Raman, Optical-Absorption, and Transmission Electron Microscopy Study of Size Effects in Germanium Quantum Dots. *Appl. Phys. Lett.* **1996**, *69*, 2409−2411.
(51) Tauc, J.; Grigorovici, R.; Vancu, A. Optical Properties and Electronic Structure of Amorphous Germanium. *Phys. Status Solidi B* **1966**, *15*, 627−637.
(52) Tauc, J. Optical Properties and Electronic Structure of Amorphous Ge and Si. *Mater. Res. Bull.* **1968**, *3*, 37−46.
(53) Takeoka, S.; Fujii, M.; Hayashi, S.; Yamamoto, K. Size-Dependent near-Infrared Photoluminescence from Ge Nanocrystals Embedded in SiO2 Matrices. *Phys. Rev. B* **1998**, *58*, 7921−7925.
(54) Barbagiovanni, E. G.; Lockwood, D. J.; Simpson, P. J.; Goncharova, L. V. Quantum Confinement in Si and Ge Nanostructures. *J. Appl. Phys.* **2012**, *111*, No. 034307.
(55) Trwoga, P. F.; Kenyon, A. J.; Pitt, C. W. Modeling the Contribution of Quantum Confinement to Luminescence from Silicon Nanoclusters. *J. Appl. Phys.* **1998**, *83*, 3789−3794.
(56) Niquet, Y. M.; Allan, G.; Delerue, C.; Lannoo, M. Quantum Confinement in Germanium Nanocrystals. *Appl. Phys. Lett.* **2000**, *77*, 1182−1184.
(57) Cosentino, S.; Barbagiovanni, E. G.; Crupi, I.; Miritello, M.; Nicotra, G.; Spinella, C.; Pacifici, D.; Mirabella, S.; Terrasi, A. Size Dependent Light Absorption Modulation and Enhanced Carrier Transport in Germanium Quantum Dots Devices. *Sol. Energy Mater. Sol. Cells* **2015**, *135*, 22−28.
(58) Kobayashi, M.; Thareja, G.; Ishibashi, M.; Sun, Y.; Griffin, P.; McVittie, J.; Pianetta, P.; Saraswat, K.; Nishi, Y. Radical Oxidation of Germanium for Interface Gate Dielectric GeO 2 Formation in Metal-Insulator-Semiconductor Gate Stack. *J. Appl. Phys.* **2009**, *106*, No. 104117.
(59) Millo, O.; Balberg, I.; Azulay, D.; Purkait, T. K.; Swarnakar, A. K.; Rivard, E.; Veinot, J. G. C. Direct Evaluation of the Quantum Confinement Effect in Single Isolated Ge Nanocrystals. *J. Phys. Chem. Lett.* **2015**, *6*, 3396−3402.

https://dx.doi.org/10.1021/acs.chemmater.9b05076
Chem. Mater. 2020, 32, 1627−1635